Article

Supramammillary Nucleus Modulates Spike-Time Coordination in the Prefrontal-Thalamo-Hippocampal Circuit during Navigation

Highlights

- Neurons in mPFC and NR increase coherence with the CA1 theta during route decisions

- Neurons in SUM change preferred spike phases to the CA1 theta on the stem of a T-maze

- Silencing of SUM neurons disrupts enhancement of spike-time coordination on the stem

- Theta-rhythm coordination modulates flow of trajectory information from mPFC to CA1

Authors

Hiroshi T. Ito, Edvard I. Moser,
May-Britt Moser

Correspondence

hiroshi.ito@brain.mpg.de (H.T.I.),
may-britt.moser@ntnu.no (M.-B.M.)

In Brief

Ito et al. show that the supramammillary nucleus in the hypothalamus is a key node to control theta-frequency spike-time coordination in the mPFC-NR-CA1 circuit. This coordination enhances the transfer of trajectory information from the prefrontal cortex to the hippocampus during route decisions.

CellPress

Article

Supramammillary Nucleus Modulates Spike-Time Coordination in the Prefrontal-Thalamo-Hippocampal Circuit during Navigation

Hiroshi T. Ito,[1,2,3,*] Edvard I. Moser,[1] and May-Britt Moser[1,*]
[1]Kavli Institute for Systems Neuroscience, Norwegian University of Science and Technology, Olav Kyrres Gate 9, MTFS, 7489 Trondheim, Norway
[2]Max Planck Institute for Brain Research, Max von Laue Str. 4, 60438 Frankfurt am Main, Germany
[3]Lead Contact
*Correspondence: hiroshi.ito@brain.mpg.de (H.T.I.), may-britt.moser@ntnu.no (M.-B.M.)
https://doi.org/10.1016/j.neuron.2018.07.021

SUMMARY

During navigation, hippocampal spatial maps are thought to interact with action-planning systems in other regions of cortex. We here report a key role for spike-time coordination in functional coupling of the medial prefrontal cortex (mPFC) to the hippocampus through the thalamic nucleus reuniens (NR). When rats perform a T-maze alternation task, spikes of neurons in mPFC and NR exhibit enhanced coordination to the CA1 theta rhythm before the choice point on the maze. A similar coordination to CA1 theta rhythm was observed in neurons of the supramammillary nucleus (SUM). Optogenetic silencing of SUM neurons reduced the temporal coordination in the mPFC-NR-CA1 circuit. Following SUM inactivation, trajectory representations were impaired in both NR and CA1, but not in mPFC, indicating a failure in transmission of action plans from mPFC to the hippocampus. The findings identify theta-frequency spike-time coordination as a mechanism for gating of information flow in the mPFC-NR-CA1 circuit.
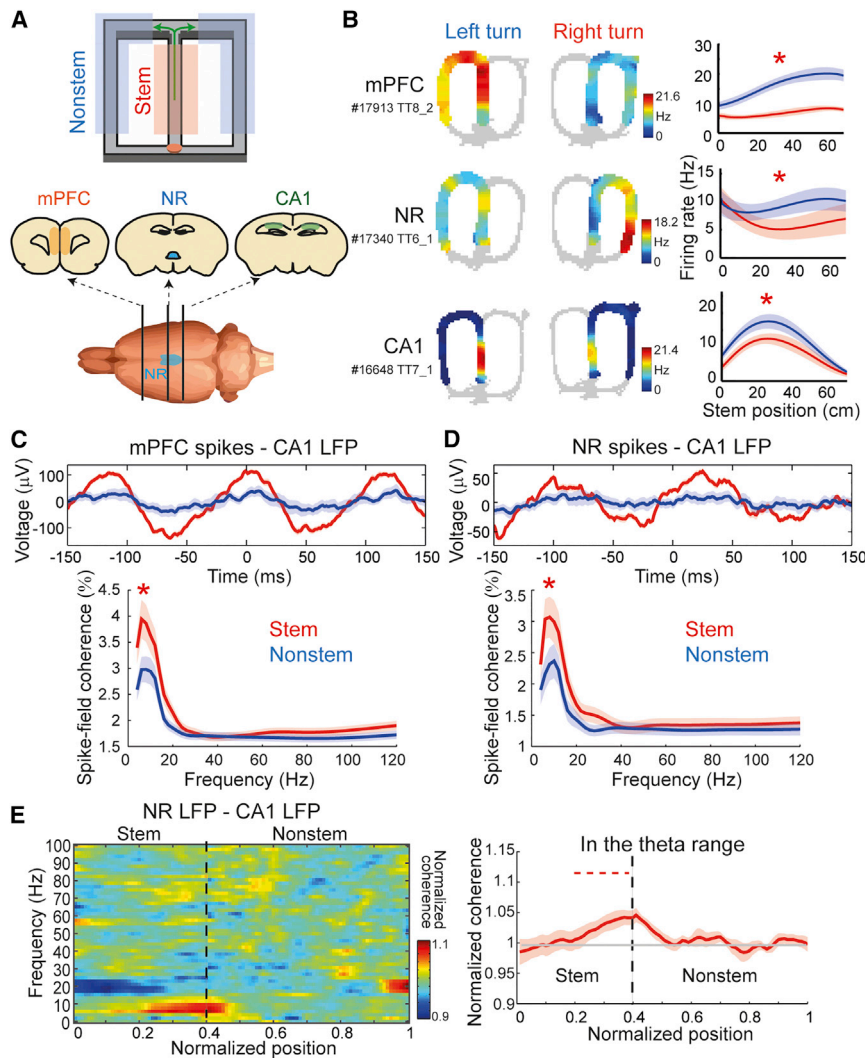
INTRODUCTION

The hippocampus and associated parahippocampal structures are key elements of the brain circuit that enables animals to navigate to desired locations in space (O'Keefe, 1991; Moser et al., 2008). Many neurons in this circuit, such as place cells or grid cells, fire when animals visit particular locations (O'Keefe and Dostrovsky, 1971; Hafting et al., 2005), suggesting that these neurons are part of an internal map of the environment. However, while place cells or grid cells provide accurate representations of the animal's instantaneous position (Mathis et al., 2012; Stemmler et al., 2015), such information alone is not sufficient for goal-directed navigation. Route planning requires encoding of not only present but also subsequent locations along trajectories. Previous studies have reported that place cells in the hippocam-

pus represent such relationships by changing their firing rates and firing sequences depending on the animal's next choice of trajectory (Frank et al., 2000; Wood et al., 2000; Johnson and Redish, 2007; Pfeiffer and Foster, 2013). Our own work has further shown that information about upcoming trajectories in the CA1 area of the hippocampus is transferred from the medial prefrontal cortex (mPFC) through the thalamic nucleus reuniens (NR) (Ito et al., 2015), which has strong projections to the CA1 region (Herkenham, 1978; Wouterlood et al., 1990; Vertes et al., 2007; Cassel et al., 2013). Such multiregional interactions may be necessary for animals to perform complex goal-directed spatial navigation tasks.

However, while long-range anatomical connections enable multiregional interactions (Bullmore and Sporns, 2009), such interactions must be dynamic to cope with changing behavioral demands. Cortical synchrony has been proposed as a mechanism for behavior-dependent functional coupling of neural circuits (Singer, 1993; Engel et al., 2001). Synchrony can be measured as phase coherence of oscillatory activity across brain regions. At the cellular level, the activity of excitatory and inhibitory neurons, firing at particular phases of neural oscillations, creates periodic time windows in which synaptic inputs have stronger or weaker impact (Singer, 1993; Buzsáki, 2002; Perez-Orive et al., 2002; Klausberger et al., 2003), such that the spike phase of afferent inputs determines the efficacy of signal transfer. Phase coherence changes dynamically depending on behavioral demands (Gregoriou et al., 2009; Fries, 2015) and through learning (Igarashi et al., 2014). How such behavior-dependent modulation of synchrony emerges is, however, largely unknown.

In the CA1 area of the hippocampus, theta-band oscillations (6–12 Hz) have been shown to be phase coupled with spike timing of neurons in mPFC (Siapas et al., 2005; Hyman et al., 2005). This temporal coordination is further enhanced when animals make a decision about where to go next at an upcoming T-junction of a maze (Jones and Wilson, 2005; Benchenane et al., 2010). Because mPFC is considered a key region for action planning and behavioral decisions (Kim and Shadlen, 1999; Mushiake et al., 2009; Simon et al., 2015), this enhancement has been proposed as a mechanism for transfer of spatial information from CA1 to mPFC for trajectory decisions during navigation. However, mPFC receives only weak input from the dorsal

Figure 1. Theta-Rhythm Coordination in the mPFC-NR-CA1 Circuit Is Enhanced before the Choice Point on a Continuous Alternation Task.

(A) Top: illustration of the maze used for a continuous alternation task. The stem region (pink) is defined as a part of the track where animals took shared trajectories between right- and left-oriented runs, before the choice point at the T-junction (green arrows). Parts of the stem where the two trajectories diverged significantly were excluded. The nonstem part (light blue) is the rest of the maze after the turn at the T-junction, but it excludes the bottom arm. The reward delivery site is indicated by an orange circle. Bottom: scheme of brain regions constituting the prefrontal-thalamo-hippocampal circuit. mPFC, medial prefrontal cortex; NR, nucleus reuniens.

(B) Representative activity of neurons in mPFC, NR, and CA1 when animals performed the continuous alternation task. Left two columns show color-coded plots of firing rates when the animal took either a left- or a right-oriented trajectory. Right column shows firing rates of the same neurons on the stem with means (solid lines) and SEM (shaded color) for a left (blue) or a right (red) trajectory (*p < 0.05 in ANOVA and ANCOVA).

(C) Top: spike-triggered LFP average on the stem and nonstem. CA1 LFP segments were 300 ms long and centered at spike timing of a representative mPFC cell. Bottom: spike-field coherence on the stem (red) and nonstem (blue) parts of the task, with means (solid lines) and SEM (shaded color) across all recorded mPFC cells (*p < 0.05 in Wilcoxon sign-rank test).

(D) The same as (C), but for NR spikes and the CA1 LFP.

(E) Left: color-coded plot of spectral coherence between LFPs in NR and CA1. Each trial position was normalized so that the position from 0 to 0.4 corresponds to when the animals were on the stem, and the position from 0.4 to 1 to when the animals were on the nonstem part of the maze.

Coherence was normalized to the average on the nonstem region. Right: same data as the left, but the plot focuses on the theta frequency band (6–12 Hz), with means (solid lines) and SEM (shaded color) across animals (red dotted line indicates the position with significantly larger coherence compared to the average coherence on the nonstem region; p < 0.05 in Friedman test).

hippocampus (Jay and Witter, 1991; Hoover and Vertes, 2007) despite the likely contribution of this part of the hippocampus in fine-scale spatial representation (Jung et al., 1994; Kjelstrup et al., 2008) and spatial learning (Nadel, 1968; Moser et al., 1993). More recent data have suggested that trajectory planning depends instead, or in addition, on transmission in the reverse direction, from mPFC via NR to CA1 (Ito et al., 2015). Here, we first asked whether coordination of neural activity in the theta frequency band is necessary for information transfer in this direction of the circuit when animals perform a continuous alternation task in a modified T-maze. Second, we examined whether this coordination is controlled by inputs from the supramammillary nucleus (SUM) in the hypothalamus, a brain region that provides theta-rhythmic inputs to all stages of the circuit—mPFC, NR, and the hippocampus (Amaral and Cowan, 1980; Haglund et al., 1984; Vertes, 1992; Vertes et al., 1995; McKenna and Vertes, 2004).

RESULTS

Enhanced Theta-Frequency Coordination between mPFC, NR, and CA1 Neurons before Trajectory Decisions

We first asked whether temporal spike coordination is observed in neurons in mPFC at the time when animals make decisions about subsequent trajectories in a continuous alternation task on a modified T-maze with return paths (Figure 1A) (Ito et al., 2015). In this task, neurons in mPFC, NR, and CA1 are known to exhibit trajectory-dependent rate changes on the stem part of the maze (Figure 1B) (Ito et al., 2015). We divided each trial on the maze into two parts based on the animal's position, distinguishing between the stem part and the rest, referred to as the nonstem part (Figure 1A). On the stem, animals are thought to prepare for an upcoming trajectory choice at the T-junction. Route planning is believed to be less predominant on the nonstem part.

In three rats trained to perform the alternation task, we recorded the activity of 329 cells from mPFC together with local field potentials (LFP) in the CA1 pyramidal layer. To test whether spike times of mPFC neurons change relative to the CA1 LFP during trajectory decisions, as reported previously in other behavioral tasks (Jones and Wilson, 2005; Benchenane et al., 2010), we measured spike-field coherence (Fries et al., 2001; Rutishauser et al., 2010) when the animals were on either the stem or the nonstem part of the maze. In these analyses, there was a significant enhancement of coherence between mPFC spikes and CA1 LFP in the theta frequency range on the stem compared with the nonstem region (spike-field coherence in 6–12 Hz [coherence × 100%]: stem 3.65% ± 0.32%, nonstem 2.86% ± 0.23%, stem/nonstem coherence ratio of individual cells = 1.44 ± 0.08; z = 2.54, p = 0.011; mean ± SEM, Wilcoxon sign-rank test; Figure 1C), indicating that mPFC spikes exhibit enhanced phase locking to the CA1 theta before the decision point on the maze. Similar results were obtained with a method based on a Hilbert transform to assess spike-phase coordination (mean vector length in 6–12 Hz: stem 0.158 ± 0.006, nonstem 0.141 ± 0.005; z = 2.79, p = 0.005, mean ± SEM, Wilcoxon sign-rank test). We did not find significant differences between stem and nonstem regions in higher frequency ranges (slow gamma [25–45 Hz]: z = 0.965, p = 0.335; fast gamma [65–90 Hz]: z = 1.77, p = 0.077). To exclude a possible influence of the animal's running speed, we analyzed spike-phase coordination based on subsampled spikes so that the mean running speed at the time of spiking was the same between the two regions (Figure S1A). Spike-phase coordination was not reduced by this equalization procedure (mean vector length in 6–12 Hz; stem 0.155 ± 0.006, nonstem 0.140 ± 0.005; z = 2.65, p = 0.008; mean ± SEM, Wilcoxon sign-rank test). There was no significant difference in overall firing rates of the mPFC-cell population between stem and nonstem parts of the maze (mean firing rates: stem 6.60 ± 0.41 Hz, nonstem 6.37 ± 0.43 Hz; z = 0.41, p = 0.68; mean ± SEM, Wilcoxon sign-rank test), suggesting that spike-time coordination is a key mechanism for behavior-dependent modulation in mPFC.

We next asked whether also NR neurons are temporally modulated during trajectory decisions. We investigated spike-time coordination between NR and CA1 in eight animals with tetrodes implanted in both NR and CA1. The activity of 91 NR cells, together with LFP in the CA1 pyramidal layer, was recorded on the T-maze. Spike-field coherence was found to be significantly enhanced in the theta frequency band on the stem compared to the nonstem region (coherence at 6–12 Hz: stem 2.94% ± 0.32%, nonstem 2.22% ± 0.26%, stem/nonstem coherence ratio of individual cells = 1.70 ± 0.16; mean ± SEM, z = 2.74, p = 0.006, Wilcoxon sign-rank test; Figure 1D). A similar result was obtained when a Hilbert transform was employed to assess spike-phase coordination (mean vector length at 6–12 Hz: stem 0.159 ± 0.008, nonstem 0.133 ± 0.007; mean ± SEM, z = 3.34, p < 0.001, Wilcoxon sign-rank test). We did not find significant differences in higher frequency ranges (slow gamma [25–45 Hz]: z = 0.74, p = 0.462; fast gamma [65–90 Hz]: z = 0.70, p = 0.481, Wilcoxon sign-rank test). We obtained equivalent results when spikes were subsampled to equalize mean running speed at spike times between stem and nonstem re-

gions (mean vector length at 6–12 Hz; 0.168 ± 0.009, nonstem 0.145 ± 0.009; mean ± SEM, z = 2.74, p = 0.006). We did not find any significant difference in overall firing rates of the NR-cell population between the stem and the nonstem parts of the maze (mean firing rates: stem 4.83 ± 0.43 Hz, nonstem 4.87 ± 0.36 Hz; mean ± SEM, z = 0.48, p = 0.63, Wilcoxon sign-rank test), suggesting that behavior-dependent modulation on the stem is mediated more by spike-time coordination than by changes in average firing rates in NR.

To further confirm these observations, we analyzed spectral coherence between LFPs recorded in CA1 and NR (Figures 1E and S1C). We found a significant enhancement of theta coherence on the final part of the stem, near the choice point of the T-maze (χ^2 and p values for each of 5 equally divided position bins on the stem compared with the average coherence on the nonstem section: $\chi^2(1)$ = 0.771, 0.010, 0.467, 5.952, 5.038; p = 0.380, 0.922, 0.495, 0.015, 0.025; two-way Friedman test with position [stem/nonstem] and animal identity as factors, 3 sessions from each of 5 animals). There was no significant difference in the theta power between the stem and nonstem regions (Figure S1D). This local enhancement of theta coherence was not correlated with the animal's running speed (r = −0.41 ± 0.13; t = 1.172, p = 0.094). Taken together, the results suggest that neurons in both mPFC and NR exhibit enhanced coordination to the CA1 theta rhythm as the animal approaches the choice point, suggesting that theta-spike coordination before trajectory decisions plays a role in information transfer not only from CA1 to mPFC as previously suggested (Jones and Wilson, 2005; Siapas et al., 2005; Benchenane et al., 2010) but also in the reverse direction, from mPFC to CA1 through NR.

Enhanced Spike-Time Coordination before Decisions in Neurons of the Supramammillary Nucleus

We found enhanced theta-rhythm coordination in the mPFC-NR-CA1 circuit when animals choose their next trajectory on the stem. However, mPFC, NR, and CA1 are anatomically distant structures, which raises the question of how these three structures can be temporally coordinated. A potential mechanism is the existence of a brain region that provides inputs to all of the three structures for temporal coordination. We hypothesized that SUM in the hypothalamus might be such a structure, because SUM has projections to mPFC, NR, and hippocampal areas CA2 and dentate gyrus, which can influence CA1 (Amaral and Cowan, 1980; Haglund et al., 1984; Vertes, 1992; Vertes et al., 1995; McKenna and Vertes, 2004). We thus recorded the activity of neurons in SUM, together with LFP from CA1, in four animals (Figures 2A and S2A). A total of 96 cells were recorded from SUM. 72% of the SUM neurons exhibited significant phase modulation to the CA1 theta rhythm (69 out of 96, with a criterion of p < 0.05 on the Rayleigh test), and 40% of the cells (38 out of 96) exhibited significant rhythmicity in the theta frequency range (6–12 Hz) in spike-autocorrelation plots (Figure 2A), consistent with previous reports in anesthetized animals (Kirk and McNaughton, 1991, 1993; Kocsis and Vertes, 1994). While SUM is composed of multiple different cell types (Pan and McNaughton, 2004), we did not find a clear relationship between spike-waveform width and degree of theta modulation for individual cells (Figure S2B).
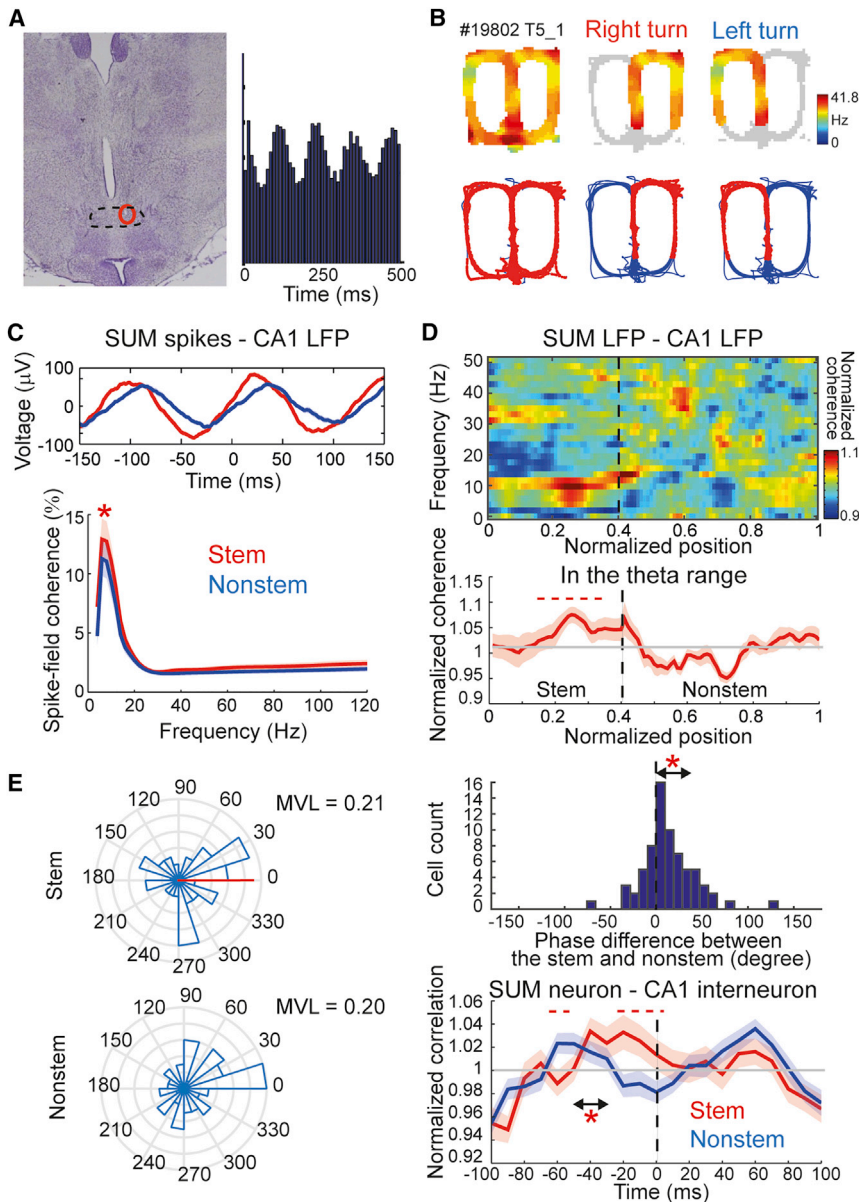
Figure 2. Neurons in SUM Exhibit Enhanced Theta-Rhythm Coordination before the Choice Point on the Stem of the Maze

(A) Nissl-stained coronal section showing tetrode track (red circle) in SUM (outline). Right panel shows a spike-autocorrelation plot of a representative cell in SUM. The cell displays theta-frequency spike modulation.

(B) Color-coded rate map of a representative cell in SUM in the continuous alternation task. Note tonic firing pattern without rate changes between trajectories on the stem.

(C) Same as Figure 1C, but for SUM spikes and the CA1 LFP.

(D) Same as Figure 1E, but for coherence between LFPs in SUM and CA1.

(E) Left: histograms of mean phases on stem or nonstem regions of the maze for theta-phase-modulated SUM neurons (69/96 cells: p < 0.05 in Rayleigh test). Red lines indicate mean phase direction for histograms with a significant phase bias (p < 0.05 in Rayleigh test). Right top: circular histograms showing phase difference between stem and nonstem regions for individual cells (*p < 0.05 in circular median test). Right bottom: spike-time cross-correlation between SUM neurons and CA1 putative interneurons on the stem (red) and nonstem (blue) regions. Time 0 on the x axis corresponds to the spike time of CA1 interneurons (*p < 0.05 in Wilcoxon sign-rank test for time shift between stem and nonstem regions). Dashed lines indicate the time when the normalized cross-correlation was significantly different between stem and nonstem regions (p < 0.05 in Wilcoxon sign-rank test).

We also assessed trajectory representations at the neural population level by a decoding approach. From each dataset, one trial was extracted as a test dataset, and the remaining trials were used as a training dataset to determine decoding parameters (leave-one-out cross-validation procedure). A population vector for each trajectory direction was constructed from the average firing rates of neurons on

We next assessed the proportion of SUM neurons that display trajectory-dependent rate changes on the stem of the T-maze. Neurons were classified as trajectory-dependent cells when their firing rates exhibited a significant (p < 0.05) main effect or interaction in a two-way ANOVA with stem positions (five position bins) and trial types (right or left) as factors and when these effects continued to be significant (p < 0.05) in a post hoc ANCOVA for factors of running speed, lateral position shift, and head direction. In contrast to mPFC, NR, and CA1, in which more than 20% of the neurons displayed trajectory-dependent rate changes on the stem of the T-maze (Ito et al., 2015), only 10% of the present SUM cells were classified as trajectory dependent (10 out of 96; Figure 2B). This percentage was not significantly different from chance level as estimated by randomly exchanging right and left trajectory trials (10.7% ± 0.9%).

the stem of the maze when animals took either a right- or a left-oriented trajectory in the training dataset (separate vectors were generated for left and right laps). We computed correlations of each of these two population vectors with a vector constructed from firing rates of the same neurons in the test dataset. The trajectory direction of the population vector that gave a higher correlation was considered as the decoded trajectory, and this direction was compared with the animal's actual choice. Decoding performance was assessed for different numbers of randomly selected neurons. Statistical distributions were determined by a bootstrap resampling procedure, and overlap with the bootstrap distributions was used to assess statistical significance. While the animal's next trajectory was well predicted from the activity of neurons in mPFC (89.4% ± 8.4% with 35 cells; Figure S2B, bottom), NR (85.2% ± 5.0%), and CA1

(98.0% ± 3.1%), the prediction made by SUM cells was at chance level (53.3% ± 15.4%), suggesting that this structure is likely not a mediator of trajectory information.

Given the lack of trajectory coding in SUM, we instead examined, for these cells, their spike-field coherence with reference to the CA1 LFP. There was a significant enhancement of SUM-CA1 coherence on the stem in the theta frequency band (6–12 Hz; stem 11.40% ± 1.48%, nonstem 9.75% ± 1.27%, stem/nonstem coherence ratio of individual cells = 1.36 ± 0.09; mean ± SEM, z = 3.48, p < 0.001, Wilcoxon sign-rank test; Figure 2C). We also found a small enhancement in the slow gamma range (25–45 Hz; stem 1.84% ± 0.17% nonstem 1.63% ± 0.12%; z = 2.27, p = 0.023, Wilcoxon sign-rank test) but no significant effect in the fast gamma range (65–90 Hz; stem 2.15% ± 0.25%; nonstem 1.78% ± 0.16%; z = 1.64, p = 0.100, Wilcoxon sign-rank test). Similar results were obtained with the Hilbert transform-based method (mean vector length in 6–12 Hz; stem 0.305 ± 0.024, nonstem 0.279 ± 0.023; mean ± SEM, z = 3.03, p = 0.003, Wilcoxon sign-rank test). The results did not change after equalization of mean running speed at the time of spiking between stem and nonstem regions (mean vector length: stem 0.263 ± 0.023, nonstem 0.231 ± 0.022; z = 3.48, p < 0.001, Wilcoxon sign-rank test). We also examined spectral coherence of LFPs between CA1 and SUM and found a small but significant increase in theta coherence in most segments of the second half of the stem (χ^2 and p values for each of 5 equally divided position bins on the stem compared with the average coherence on the nonstem: $\chi^2(1)$ = 0.76, 3.86, 3.86, 3.86, 3.05; p = 0.383, 0.049, 0.049, 0.049, 0.081; two-way Friedman test, 3 sessions from each of 4 animals; Figures 2D and S1C). Taken together, these observations suggest that neurons in SUM exhibit behavior-dependent spike-time coordination to the CA1 theta rhythm largely in the same way as those in mPFC and NR, consistent with the idea that SUM is a potential coordinator for the mPFC-NR-CA1 circuit.

Because overall firing rates of SUM-cell population were slightly lower on the stem of the maze (stem 9.62 ± 1.19 Hz, nonstem 9.76 ± 1.70 Hz; mean ± SEM, z = 2.07, p = 0.038; Wilcoxon sign-rank test), we hypothesized that temporal coordination of the mPFC-NR-CA1 circuit is based on the change of spike timing in SUM neurons. We thus asked whether spike phases of SUM cells to the CA1 theta differ between the stem and the nonstem parts of the maze (Figure 2E). We found that SUM cells changed their preferred spike timing to a later phase of the CA1 theta on the stem (12.3° ± 0.8°; mean ± SEM, z = 3.73, p < 0.001, circular median test). Such changes were not observed in mPFC (5.17° ± 1.8° later phase on the stem; z = 1.34, p = 0.207, circular median test; Figure S2C) or in NR (4.17° ± 2.5°; z = 1.48, p = 0.177). We also examined spike-time cross-correlations of pairs of SUM neurons and CA1 putative interneurons (Figure 2E, bottom right). While SUM neurons exhibited low firing at the spike time of CA1 interneurons in the nonstem region (normalized SUM-spike correlation at the spike time of CA1 interneurons: 0.981 ± 0.009), their spike time shifted significantly on the stem (15.6 ± 5.9 ms, z = 2.56, p = 0.010 in Wilcoxon sign-rank test), and SUM cells began to fire near the spike time of the CA1 interneurons (normalized SUM-spike correlation at the spike time of CA1 interneurons: 1.014 ± 0.013; z = 2.15, p = 0.031 in Wilcoxon sign-rank

test for comparison of correlations between stem and nonstem). These results imply that SUM cells could dynamically coordinate the mPFC-NR-CA1 circuit by changing their spike timing relative to the CA1 theta.

SUM Inactivation Disrupts Theta-Spike Coordination in the mPFC-NR-CA1 Circuit

Our results indicate a possible role for SUM in temporal coordination of the mPFC-NR-CA1 circuit during trajectory decisions. To explicitly test this idea, we inactivated neurons in SUM using optogenetic tools. We injected AAV2 encoding eArch3.0 (Mattis et al., 2011) in SUM, and an optical fiber was targeted at approximately 500 μm above SUM, so that 532 nm laser application reduced the activity of SUM neurons (Figure 3A). Three of the animals had tetrodes implanted in mPFC and CA1 (Figure S3), and four had tetrodes in NR and CA1 (Figure S4). We first examined spectral coherence between NR and CA1 LFPs. Theta coherence was enhanced on the stem before laser application, as observed in different animals in the previous experiment (Figure 1E). When light was applied to SUM from the beginning to the end of each trial, we observed a consistent reduction of theta coherence on the stem of the maze, which recovered when the laser application was terminated (χ^2 and p values for each of the 5 position bins on the stem before, during, and after laser application: $\chi^2(2)$ = 12.42, 12.29, 12.16, 9.62, 2.87; p = 0.002, 0.002, 0.002, 0.008, 0.239; two-way Friedman test with session type and animal identity as factors, 3 sessions from each of 4 animals, p < 0.05 in a post hoc test between before and laser; Figure 3B). Similar changes were not found in the nonstem region (χ^2 and p values for each of the 5 equally divided bins on the nonstem: $\chi^2(2)$ = 2.42, 1.76, 0.42, 3.09, 1.67; p = 0.298, 0.416, 0.810, 0.213, 0.435; two-way Friedman test), suggesting a selective role of SUM in theta-rhythm coordination between NR and CA1 near the choice point on the T-maze.

We next analyzed the impact of SUM silencing on spike-time coordination of neurons in mPFC and NR with LFP in CA1. Before laser application, we found significant enhancement of spike-field coherence in the theta frequency range on the stem region in both mPFC and NR neurons, as observed in different animals in the previous experiments (mPFC: stem 3.41% ± 0.35%, nonstem 3.07% ± 0.36%; mean ± SEM, z = 2.31, p = 0.021; NR: stem 2.02% ± 0.18% nonstem 1.67% ± 0.13%; z = 2.89, p = 0.004; Wilcoxon sign-rank test; Figure 3C). Laser application disrupted this modulation of spike-field coherence (mPFC: stem 2.76% ± 0.33%, nonstem 2.73% ± 0.32%; z = 0.74, p = 0.460; NR: stem 1.76% ± 0.14%, nonstem 1.54% ± 0.10%; z = 1.28, p = 0.200). When the laser was turned off, the enhancement of spike-field coherence on the stem showed partial recovery (mPFC: stem 3.19% ± 0.35%, nonstem 3.03% ± 0.34%; z = 0.975, p = 0.329; NR: stem 1.99% ± 0.17%, nonstem 1.67% ± 0.15%; z = 2.60, p = 0.009). The reduction of coherence during SUM inactivation was not merely a consequence of disruption of theta rhythmicity in mPFC or NR; spike-field locking to local theta in these regions was largely maintained during the inactivation, and the reduction of local coherence was significantly smaller than coherence to CA1 theta (spike-field coherence on the stem to local theta; mPFC: before
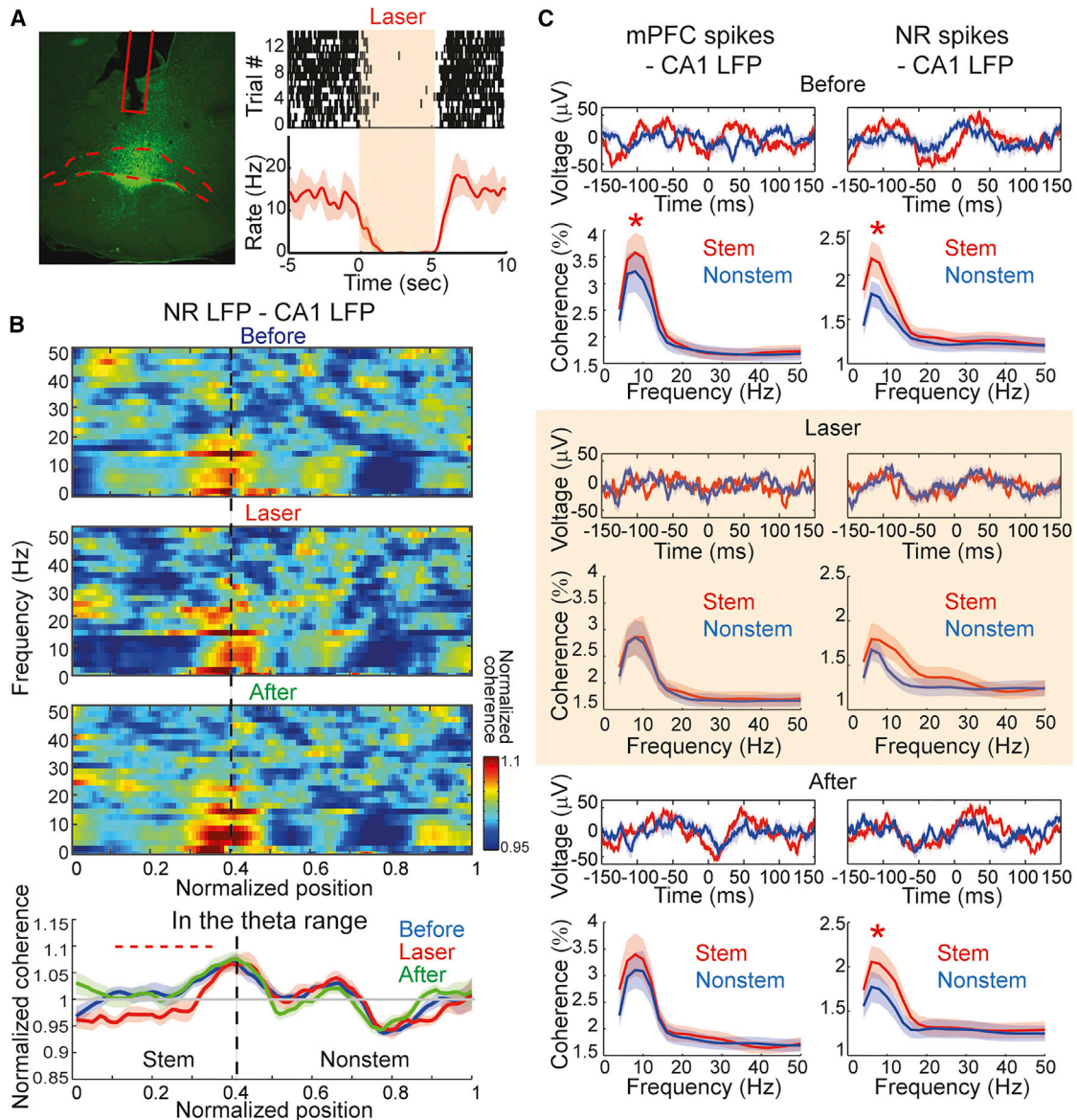
Figure 3. SUM Inactivation Impairs Theta-Rhythm Coordination on the Stem of the Maze

(A) Immunostained coronal brain section showing the expression of eArch3.0 (green) in SUM (outline) as well as an optic fiber location (red rectangle). Right panels show spike raster (top) and rate plot (bottom) of a representative SUM cell. Laser illumination at 532 nm was applied from 0 to 5 s.

(B) Top: color-coded spectral coherence plots between LFPs in NR and CA1 for sessions before, during, and after laser application. Coherence was normalized to the average on the nonstem region. Bottom: same data as the top, but the plot focuses on the theta range of frequency, showing means (solid lines) and SEM (shaded) across animals for before (blue), laser (red), and after (green) sessions (red dotted line indicates the position with p < 0.05 in Friedman test as well as a post hoc test between before and laser).

(C) Spike-triggered LFP averages and spike-field coherence plots for neurons in mPFC or NR to the CA1 LFP. The analyses were performed on the same population of neurons with the same spike number across sessions using a subsampling procedure (*p < 0.05 in Wilcoxon sign-rank test).

2.24% ± 0.19%, during 2.08% ± 0.16%, after 2.23% ± 0.20%; $\chi^2(1) = 17.7$, p < 0.001 for comparison of coherence to local versus CA1 theta by two-way Friedman test with theta source [CA1/local] and session type [before, laser, after] as factors; NR: before 1.61% ± 0.12%, during 1.57% ± 0.12%, after 1.64% ± 0.12%; $\chi^2(1) = 5.48$, p = 0.019; Figure S5B). We also assessed the degree of phase precession of CA1 place cells to test whether theta-rhythm spike-coordination in CA1 is affected by SUM inactivation. We did not see any significant change in slopes of phase precession during laser application (slopes estimated by circular-linear regression on phase-position plots; before −3.01 ± 0.44 degree/cm, during −2.43 ± 0.49 degree/cm, after −2.40 ± 0.44 degree/cm; $\chi^2(2) = 0.46$, p = 0.793, Kruskal-Wallis test). The results together suggest that SUM plays an
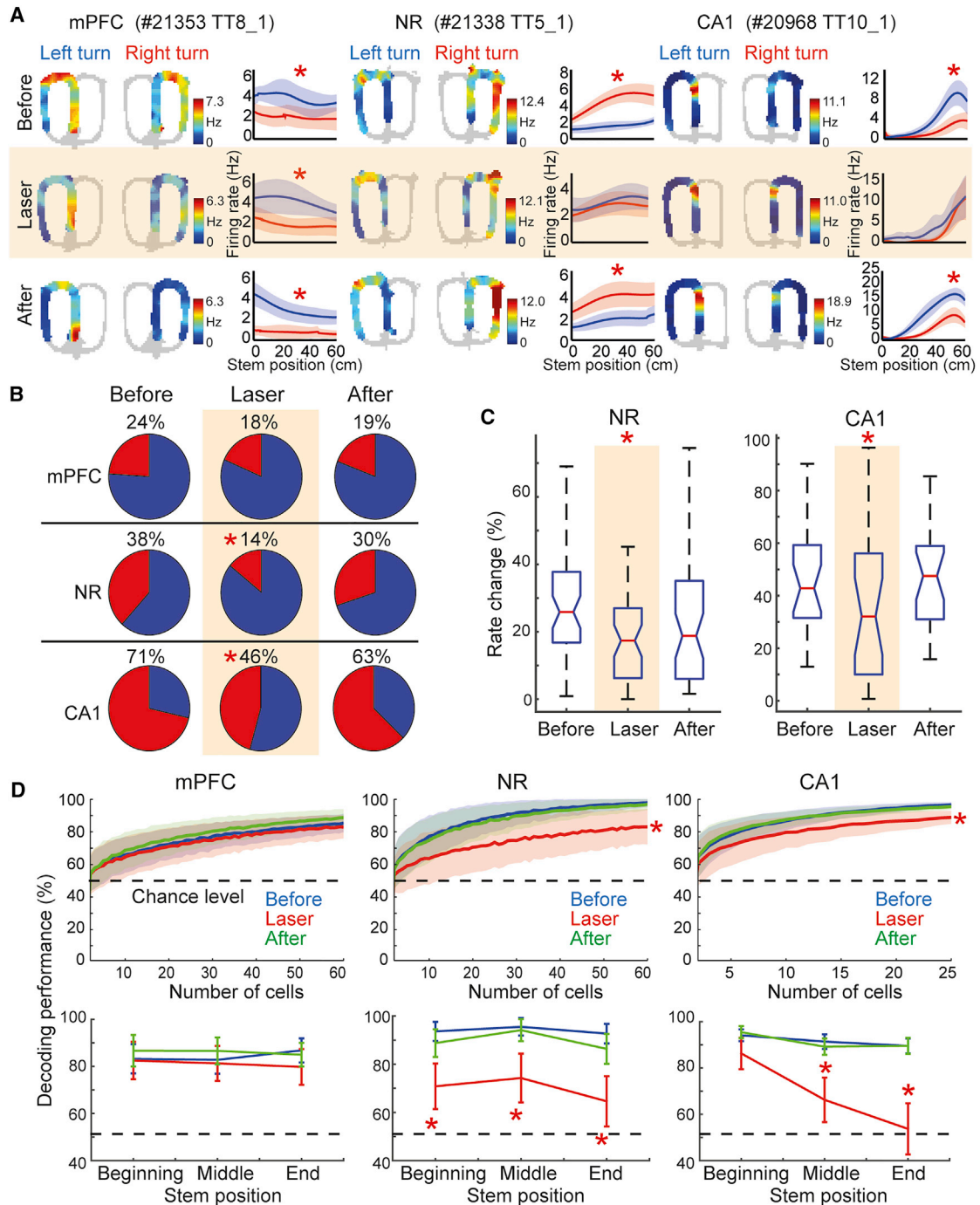
Figure 4. SUM Inactivation Impairs Trajectory Representations in NR and CA1

(A) Color-coded rate maps of a representative cell in mPFC, NR, or CA1 displaying when the animal took a left-oriented or right-oriented trajectory, respectively. Rate plots to the right show mean firing rates (solid lines) and SEM (shaded) of the same cells on the stem for a right (red) and a left (blue) trajectory (*p < 0.05 in ANOVA and ANCOVA).

(B) Pie charts showing proportion of trajectory-dependent cells (red) in mPFC, NR, or CA1 (*p < 0.05 in binomial test).

(C) Normalized change of firing rates between trajectories ([$high - low$]/$high$) across sessions, before, during, and after laser application (*p < 0.05 in Friedman test as well as post hoc Wilcoxon sign-rank test between before and laser).

(D) Decoding performance of the animal's next trajectory choice from population activity of neurons in mPFC, NR, or CA1 on the stem. Top: a statistical distribution of the performance was estimated by a bootstrap resampling method for different cell numbers. Each plot shows mean decoding performance

(legend continued on next page)

essential role in coordination of theta-modulated spike activity in the mPFC-NR-CA1 circuit before trajectory decisions.

SUM Inactivation Disrupts Trajectory Representation in NR and CA, but Not mPFC

Our results point to a key role for SUM in behavior-dependent theta-rhythm coordination in the mPFC-NR-CA1 circuit. What then is the functional impact of this spike coordination on neuronal representations in the circuit? Our previous study suggested that the mPFC-NR-CA1 circuit is crucial for transfer of information from mPFC to CA1 about the next steps of the trajectory (Ito et al., 2015). We thus examined the impact of SUM inactivation on trajectory-dependent rate changes of neurons in the mPFC-NR-CA1 circuit. We recorded 146 mPFC cells from the animals with tetrodes implanted in mPFC and 120 NR cells and 114 CA1 cells from the animals with tetrodes in NR and CA1. Among the CA1 cells, 35 cells exhibited location-selective activity on the stem part of the maze. We compared firing rates of cells on the stem when animals took either a right-oriented or a left-oriented trajectory at the upcoming T-junction. Cells that exhibited a significant rate change between trajectories on the stem, which could not be explained by the animal's head direction, lateral position, or running speed on the track, were categorized as trajectory-dependent cells.

SUM inactivation did not significantly change the proportion of trajectory-dependent cells in mPFC (before 35/146 = 24%, during 27/146 = 18%, after 28/146 = 19%; t = 1.145, p = 0.252, binomial test between before and laser; Figures 4A and 4B). However, the inactivation led to a significant reduction of the fraction of trajectory-dependent cells in NR (before 46/120 = 38%, during 17/120 = 14%, after 36/120 = 30%; t = 4.25, p < 0.001, binomial test between before and laser; Figures 4A and 4B) and in CA1 (before 25/35 = 71%, during 16/35 = 46%, after 22/35 = 63%; t = 2.18, p = 0.029, binomial test between before and laser). In mPFC, there was no significant firing rate change between trajectories (before 29.9% ± 3.4%, during 19.8% ± 3.0%, after 27.6% ± 3.7%; mean ± SEM, $\chi^2(2)$ = 5.02, p = 0.081, one-way Friedman test), but there was a significant reduction of the trajectory-dependent rate change in NR (Figure 4C; before 28.1% ± 2.2%, during 17.3% ± 1.8%, after 22.4% ± 2.6%; $\chi^2(2)$ = 20.2, p < 0.001, one-way Friedman test; p < 0.05 in a post hoc Wilcoxon sign-rank test between before and laser) and in CA1 (before 46.0% ± 4.1%, during 36.7% ± 5.9%, after 47.0% ± 3.8%; $\chi^2(2)$ = 10.6, p = 0.005; p < 0.05 for post hoc Wilcoxon sign-rank test).

We also assessed trajectory representations at the neural population level by a decoding approach. Decoding of the next trajectory was performed based on population vector correlations and leave-one-out cross validation, and overlap of resampled distributions was used to assess statistical significance, as described above. In mPFC, SUM inactivation did not impair decoding performance (decoding from 60 mPFC cells:
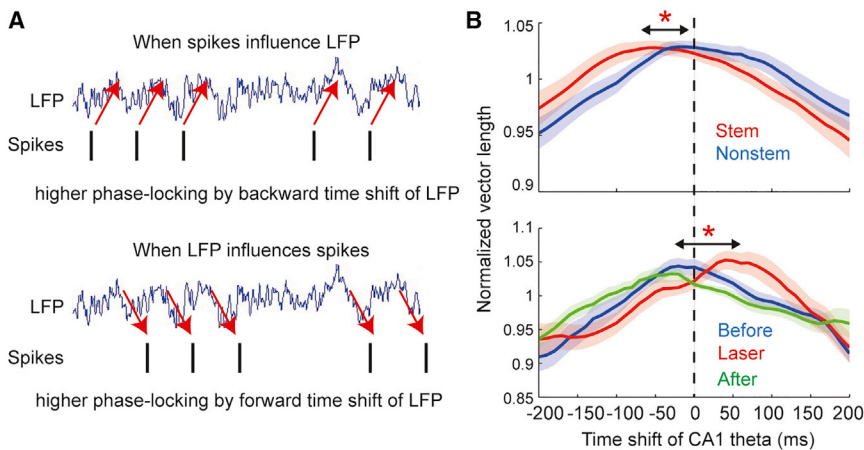
before 85.5% ± 5.7% correct, laser 83.0% ± 7.0%, after 88.7% ± 5.1%, mean ± SEM, p = 0.407; Figure 4D). However, following SUM inactivation, decoding was significantly impaired in NR (decoding performance from 60 NR cells: before 97.9% ± 2.8%, laser 83.1% ± 10.9%, after 96.9% ± 3.4%; p = 0.047) and in CA1 (decoding performance from 25 CA1 cells: before 96.6% ± 1.6%, laser 88.9% ± 4.0%, after 95.6% ± 1.9%; p = 0.020; Figure 4D). We further examined the decoding performance in three equally divided stem positions (Figure 4D, bottom). While these analyses failed to show any decoding impairment in mPFC during SUM inactivation (comparison of distributions between before and laser at each stem position: p = 0.488, 0.449, 0.329), we observed consistent impairment across stem positions in NR (p = 0.004, 0.016, 0.005). For CA1 neurons, the performance was maintained at the beginning of the stem (p = 0.115) but impaired toward the end of stem (p = 0.003 and p = 0.001). Thus, the disruption of temporal coordination by SUM inactivation impaired trajectory representations in NR and CA1. In contrast, trajectory representation in mPFC persisted, suggesting that mPFC may be the source of trajectory information, not influenced by spike-time coordination mediated by SUM.

What is the relationship of spike-time coordination to the animal's performance in the continuous alternation task? We did not find a significant change of behavioral performance during SUM inactivation (correct percent: before 98.1% ± 0.4%, during 96.5% ± 0.7%, after 96.8% ± 0.6%; mean ± SEM, $\chi^2(2)$ = 2.32, p = 0.313; one-way Friedman test). Consistent with this observation, error trials were not associated with impaired spike-time coordination of neurons in SUM or NR to the CA1 theta (SUM: correct 14.0% ± 1.9%, error 15.3% ± 2.4%; mean ± SEM, z = 0.656, p = 0.512, Wilcoxon sign-rank test; NR: correct 13.9% ± 1.7%, error 11.8% ± 2.2%; z = 1.40, p = 0.162; Figure S2D). However, there was a significant reduction of spike-time coordination of mPFC neurons to the CA1 theta on error trials (correct 8.6% ± 0.6%, error 7.2% ± 0.8%; z = 3.10, p = 0.002). These results suggest that, while SUM-mediated coordination is a key mechanism for control of information transfer from mPFC to CA1, the trajectory information itself may be formed in mPFC independently of SUM.

Modulation of Spike Impact by Theta-Rhythm Coordination

Our results suggest that spike-time coordination to the theta rhythm plays a key role in the information transfer in the mPFC-NR-CA1 circuit. Because SUM inactivation did not change the mean firing rates of mPFC or NR cells (Figure S5C), theta-rhythm coordination is likely to change the impact of individual spikes on the circuits. To test this idea, we examined the microstructure of theta-spike coordination to estimate the directionality of signal flow in the circuit (Siapas et al., 2005). We examined the degree of phase locking of neurons in mPFC,

---

(solid lines) and SEM (shaded) across sessions, before (blue), during (red), and after (green) laser application. Significant impairment of decoding performance by SUM inhibition was observed in neurons recorded in NR and CA1, but not in mPFC. Bottom: decoding performance was estimated at three equally divided positions on the stem using 60 cells from mPFC or NR and 25 cells from CA1 (*p < 0.05 in a comparison of bootstrap distributions before and laser).

A When spikes influence LFP

B

Figure 5. Change of Signal Flow from NR to CA1 during SUM Inactivation

(A) Schema showing concept of the analysis on the microstructure of spike-LFP coordination. When the spike activity in one structure has a causal impact on LFP in the other structure of the brain, higher spike-phase locking is expected by shifting the LFP trace backward in time to compensate for the effective axonal conduction delay. On the other hand, when LFP has a causal impact on the spike activity in the other brain area, higher spike-phase locking will be observed by shifting the LFP trace forward in time.

(B) Normalized mean vector length of spike phases of NR neurons relative to a series of CA1 LFP traces that were shifted from −200 ms to 200 ms at 10 ms intervals in time relative to the original trace. Top: comparison between stem (red) and nonstem (blue) regions. Bottom: comparison on the stem across sessions before (blue), during (red), and after (green) laser application. Plots show means (solid lines) and SEM (shaded) of all recorded NR cells (*p < 0.05 in Wilcoxon rank-sum test).

NR, or SUM at different temporal offsets of the CA1 theta (−200 ms to 200 ms at 10 ms intervals) using the temporal offset that gives the maximum phase locking as an indicator of the effective axonal conduction delay from one structure to another. If the spike activity in one structure has a causal influence on LFP in the other structure, higher spike-phase locking should be observed by shifting LFP traces backward in time relative to spikes to compensate for the axonal conduction delay (Figure 5A). In contrast, if LFP influences the spike activity, higher spike-phase modulation would be observed by shifting LFP traces forward in time.

We first asked whether the temporal offset that yields the maximum phase locking was different between the stem and the nonstem parts of the maze. There was no significant difference between regions in the temporal offsets of CA1 theta that gave maximum phase locking for mPFC spikes (peak shift: −3.98 ± 6.0 ms, nonstem 12.0 ± 5.3 ms; mean ± SEM, z = 1.90, p = 0.057; Wilcoxon rank-sum test; Figure S5E) or for SUM spikes (stem −13.0 ± 8.8 ms, nonstem −17.2 ± 10.4 ms; z = 0.507, p = 0.612). However, there was a significant difference in temporal offsets for NR spikes between the stem and the nonstem regions (stem −33.3 ± 11.2 ms, nonstem 2.62 ± 10.2 ms; z = 2.29, p = 0.022; Figure 5B). Maximum phase locking on the stem was obtained by shifting the CA1 theta backward in time, implying that NR spikes have a stronger impact on CA1 spike activity than CA1 theta on NR activity during trajectory decisions.

We finally examined the influence of SUM inactivation on signal flow in the mPFC-NR-CA1 circuit. While SUM inactivation did not change signal directionality between mPFC spikes and the CA1 theta (peak time shift: before 10.5 ± 10.6 ms, during −8.2 ± 12.2 ms, after 23.5 ± 11.1 ms; $\chi^2(2)$ = 4.07, p = 0.131, Kruskal-Wallis test), we found a significant change in signal directionality between NR spikes and the CA1 theta during SUM inactivation on the stem (before −0.8 ± 11.2 ms, during 33.0 ± 11.3 ms, after −10.5 ± 13.3 ms; $\chi^2(2)$ = 7.19, p = 0.027, Kruskal-Wallis test; p < 0.05 for post hoc Wilcoxon rank-sum test between before and laser; Figure 5B). During SUM inactivation, maximum phase locking of NR cells was obtained by shift-

ing the CA1 theta forward in time, implying that the directionality of signal flow was from CA1 to NR rather than from NR to CA1. We did not find a corresponding difference in the nonstem part of the maze (mPFC spike-CA1 theta: $\chi^2(2)$ = 3.69, p = 0.158; NR spike-CA1 theta: $\chi^2(2)$ = 4.35, p = 0.113, Kruskal-Wallis test). The results suggest that SUM inactivation reduces the directional impact of NR spikes to CA1 on the stem, supporting the idea that spike-time coordination determines the efficacy of information transfer between the regions.

DISCUSSION

Functional coupling between the prefrontal cortex and the hippocampus is thought to change dynamically depending on behavioral demands (Sigurdsson and Duvarci, 2016). When animals choose a trajectory during navigation, information about the planned movement direction in mPFC is integrated with hippocampal spatial maps through the mPFC-NR-CA1 circuit (Ito et al., 2015). Our present results demonstrate that information transfer in the mPFC-NR-CA1 circuit is enhanced before the choice point on the stem of a T-maze through temporal spike coordination and not by overall firing rate, which was unaltered in mPFC and NR. On the stem, near the choice point, neurons in mPFC and NR exhibited enhanced coordination to the CA1 theta. Neurons in SUM displayed a similar enhancement of spike-time coordination to the CA1 theta, and inactivation of SUM impaired the enhancement of theta coherence on the stem in the mPFC-NR-CA1 circuit. The disruption of temporal coordination reduced the transfer of the trajectory information from mPFC to CA1 through NR and, consequently, the ability of NR and CA1 neurons to differentiate upcoming trajectories. This points to theta-rhythm coordination as an important mechanism for controlling signal flow in the mPFC-NR-CA1 circuit.

SUM has long been considered a key structure for the generation of theta rhythm in the brain. SUM has reciprocal anatomical connections with the medial septum (Vertes, 1992; Hayakawa et al., 1993; Pan and McNaughton, 2004), another element of the circuit for hippocampal theta oscillations (Petsche et al.,

1962; Stumpf et al., 1962; Gogolák et al., 1968; Lee et al., 1994). In anesthetized animals, the injection of an inhibitor of neural activity, procaine, into the medial septum reduces the amplitude of theta oscillations without affecting its frequency in the hippocampus, but the theta rhythmicity of SUM cells is largely maintained (Kirk and McNaughton, 1991). In contrast, procaine injection into SUM reduces both frequency and amplitude of theta oscillations in the hippocampus (Kirk and McNaughton, 1993), suggesting that SUM is the pacemaker of the theta rhythm. However, in freely behaving animals, although lesions of the medial septum result in a large reduction of the hippocampal theta rhythm (Gray, 1971), SUM lesions fail to affect it (Thinschmidt et al., 1995), putting a role for SUM in theta rhythm generation into question. Consistent with these previous studies, we found that optogenetic inhibition of SUM did not affect the theta rhythm itself in CA1, NR, or mPFC. However, the preferred spike phases of SUM cells relative to the CA1 theta, as well as their spike-time relationships to CA1 interneurons, were changed, which further altered the degree of phase locking of these spikes to the CA1 theta. This points to a role for SUM in the creation of oscillatory interference between its own theta rhythm and the ongoing rhythm in its projection areas, which may dynamically control temporal coordination in the circuit.

While SUM inactivation impaired spike-time coordination in the mPFC-NR-CA1 circuit, as well as the transfer of rate information about upcoming trajectories, it did not significantly affect the animal's behavioral performance in the continuous alternation task. Decoding performance of the next trajectory choice was significantly impaired by SUM inactivation but was still maintained above the chance level, which may be due to incomplete silencing of SUM as the size of optical fibers was smaller than the size of SUM in the present study. This partially impaired trajectory representation may be sufficient for animals to perform the task successfully. However, even with complete inactivation of SUM, behavioral performance may not be disrupted, because in our previous work, lesions or optogenetic silencing of NR, accompanied by impairment of trajectory representation in CA1, did not affect behavioral performance in the same task (Ito et al., 2015). As animals with lesions in the hippocampus can perform this task (Ainge et al., 2007), the task likely does not require interactions of mPFC with hippocampal spatial maps. We expect, however, that such interactions will become crucial in a more complex version of the task that requires discrimination of multiple combinations of positions and trajectories, and under this situation, SUM-mediated spike-time coordination may become a key determinant of the animal's choice of a correct trajectory.

Cortical synchrony has long been considered a key mechanism for dynamic functional coupling across brain regions (Singer, 1993). A large body of evidence has demonstrated that phase coherence between brain regions is dynamically modulated depending on the task demand, which influences the efficacy of signal transfer between regions (Engel et al., 2001; Laurent, 2002; Fries, 2015; Harris and Gordon, 2015). However, it has been largely unclear how multiple distant brain structures can be coordinated together depending on behavioral demands. Because of the axonal conduction delay, it is not such a trivial issue to synchronize multiple brain areas only through

reciprocal anatomical connections between them. We here found that trajectory coding is modulated through theta-rhythm synchrony in the mPFC-NR-CA1 circuit, and we identified SUM as a structure that coordinates the theta rhythm across the circuit depending on behavioral demands. By pointing to a hypothalamic node for cortical synchronization, our study sheds light on how subcortical networks control operations and behaviors of the cortex.

STAR★METHODS

Detailed methods are provided in the online version of this paper and include the following:

- KEY RESOURCES TABLE
- CONTACT FOR REAGENT AND RESOURCE SHARING
- EXPERIMENTAL MODEL AND SUBJECT DETAILS
- METHOD DETAILS
  - Surgery, Virus Injection, Lesions, and Drive Implantation
  - Electrode Turning and Recording Procedures
  - Behavioral Task on the Modified T-Maze
  - Histological Procedures and Electrode Positions
  - Immunohistochemistry
- QUANTIFICATION AND STATISTICAL ANALYSIS
  - Spike Sorting and Cell Classification
  - Trajectory-Dependent Firing on the Modified T-Maze
  - Spike Phase Analysis
  - Spectral Coherence Analysis
  - Decoding Analysis
  - Signal Directionality Analysis
  - Theta Waveform Analysis
  - Detection of Theta Rhythmicity
- DATA AND SOFTWARE AVAILABILITY

AUTHOR CONTRIBUTIONS

H.T.I., E.I.M., and M.-B.M. designed the experiment. H.T.I. performed all experiments and analyses. H.T.I. wrote the manuscript, and E.I.M. and M.-B.M. edited and commented.

DECLARATION OF INTERESTS

The authors declare no competing interests.

SUPPORTING CITATIONS

The following reference appears in the Supplemental Information: Cole and Voytek (2017).

REFERENCES

Ainge, J.A., van der Meer, M.A., Langston, R.F., and Wood, E.R. (2007). Exploring the role of context-dependent hippocampal activity in spatial alternation behavior. Hippocampus 17, 988–1002.

Amaral, D.G., and Cowan, W.M. (1980). Subcortical afferents to the hippocampal formation in the monkey. J. Comp. Neurol. 189, 573–591.

Benchenane, K., Peyrache, A., Khamassi, M., Tierney, P.L., Gioanni, Y., Battaglia, F.P., and Wiener, S.I. (2010). Coherent theta oscillations and reorganization of spike timing in the hippocampal- prefrontal network upon learning. Neuron 66, 921–936.

Brandon, M.P., Bogaard, A.R., Schultheiss, N.W., and Hasselmo, M.E. (2013). Segregation of cortical head direction cell assemblies on alternating θ cycles. Nat. Neurosci. 16, 739–748.

Bullmore, E., and Sporns, O. (2009). Complex brain networks: graph theoretical analysis of structural and functional systems. Nat. Rev. Neurosci. 10, 186–198.

Buzsáki, G. (2002). Theta oscillations in the hippocampus. Neuron 33, 325–340.

Cassel, J.C., Pereira de Vasconcelos, A., Loureiro, M., Cholvin, T., Dalrymple-Alford, J.C., and Vertes, R.P. (2013). The reuniens and rhomboid nuclei: neuroanatomy, electrophysiological characteristics and behavioral implications. Prog. Neurobiol. 111, 34–52.

Cole, S.R., and Voytek, B. (2017). Brain oscillations and the importance of waveform shape. Trends Cogn. Sci. 21, 137–149.

Cole, S.R., van der Meij, R., Peterson, E.J., de Hemptinne, C., Starr, P.A., and Voytek, B. (2017). Nonsinusoidal beta oscillations reflect cortical pathophysiology in Parkinson's disease. J. Neurosci. 37, 4830–4840.

Colgin, L.L., Denninger, T., Fyhn, M., Hafting, T., Bonnevie, T., Jensen, O., Moser, M.B., and Moser, E.I. (2009). Frequency of gamma oscillations routes flow of information in the hippocampus. Nature 462, 353–357.

Csicsvari, J., Hirase, H., Czurkó, A., Mamiya, A., and Buzsáki, G. (1999). Oscillatory coupling of hippocampal pyramidal cells and interneurons in the behaving rat. J. Neurosci. 19, 274–287.

Engel, A.K., Fries, P., and Singer, W. (2001). Dynamic predictions: oscillations and synchrony in top-down processing. Nat. Rev. Neurosci. 2, 704–716.

Frank, L.M., Brown, E.N., and Wilson, M. (2000). Trajectory encoding in the hippocampus and entorhinal cortex. Neuron 27, 169–178.

Fries, P. (2015). Rhythms for cognition: communication through coherence. Neuron 88, 220–235.

Fries, P., Reynolds, J.H., Rorie, A.E., and Desimone, R. (2001). Modulation of oscillatory neuronal synchronization by selective visual attention. Science 291, 1560–1563.

Gogolák, G., Stumpf, C., Petsche, H., and Sterc, J. (1968). The firing pattern of septal neurons and the form of the hippocampal theta wave. Brain Res. 7, 201–207.

Gray, J.A. (1971). Medial septal lesions, hippocampal theta rhythm and the control of vibrissal movement in the freely moving rat. Electroencephalogr. Clin. Neurophysiol. 30, 189–197.

Gregoriou, G.G., Gotts, S.J., Zhou, H., and Desimone, R. (2009). Long-range neural coupling through synchronization with attention. Prog. Brain Res. 176, 35–45.

Hafting, T., Fyhn, M., Molden, S., Moser, M.B., and Moser, E.I. (2005). Microstructure of a spatial map in the entorhinal cortex. Nature 436, 801–806.

Haglund, L., Swanson, L.W., and Köhler, C. (1984). The projection of the supramammillary nucleus to the hippocampal formation: an immunohistochemical and anterograde transport study with the lectin PHA-L in the rat. J. Comp. Neurol. 229, 171–185.

Harris, A.Z., and Gordon, J.A. (2015). Long-range neural synchrony in behavior. Annu. Rev. Neurosci. 38, 171–194.

Hayakawa, T., Ito, H., and Zyo, K. (1993). Neuroanatomical study of afferent projections to the supramammillary nucleus of the rat. Anat. Embryol. (Berl.) 188, 139–148.

Herkenham, M. (1978). The connections of the nucleus reuniens thalami: evidence for a direct thalamo-hippocampal pathway in the rat. J. Comp. Neurol. 177, 589–610.

Hoover, W.B., and Vertes, R.P. (2007). Anatomical analysis of afferent projections to the medial prefrontal cortex in the rat. Brain Struct. Funct. 212, 149–179.

Hyman, J.M., Zilli, E.A., Paley, A.M., and Hasselmo, M.E. (2005). Medial prefrontal cortex cells show dynamic modulation with the hippocampal theta rhythm dependent on behavior. Hippocampus 15, 739–749.

Igarashi, K.M., Lu, L., Colgin, L.L., Moser, M.B., and Moser, E.I. (2014). Coordination of entorhinal-hippocampal ensemble activity during associative learning. Nature 510, 143–147.

Ito, H.T., Zhang, S.J., Witter, M.P., Moser, E.I., and Moser, M.B. (2015). A prefrontal-thalamo-hippocampal circuit for goal-directed spatial navigation. Nature 522, 50–55.

Jay, T.M., and Witter, M.P. (1991). Distribution of hippocampal CA1 and subicular efferents in the prefrontal cortex of the rat studied by means of anterograde transport of Phaseolus vulgaris-leucoagglutinin. J. Comp. Neurol. 313, 574–586.

Johnson, A., and Redish, A.D. (2007). Neural ensembles in CA3 transiently encode paths forward of the animal at a decision point. J. Neurosci. 27, 12176–12189.

Jones, M.W., and Wilson, M.A. (2005). Theta rhythms coordinate hippocampal-prefrontal interactions in a spatial memory task. PLoS Biol. 3, e402.

Jung, M.W., Wiener, S.I., and McNaughton, B.L. (1994). Comparison of spatial firing characteristics of units in dorsal and ventral hippocampus of the rat. J. Neurosci. 14, 7347–7356.

Kempter, R., Leibold, C., Buzsáki, G., Diba, K., and Schmidt, R. (2012). Quantifying circular-linear associations: hippocampal phase precession. J. Neurosci. Methods 207, 113–124.

Kim, J.N., and Shadlen, M.N. (1999). Neural correlates of a decision in the dorsolateral prefrontal cortex of the macaque. Nat. Neurosci. 2, 176–185.

Kirk, I.J., and McNaughton, N. (1991). Supramammillary cell firing and hippocampal rhythmical slow activity. Neuroreport 2, 723–725.

Kirk, I.J., and McNaughton, N. (1993). Mapping the differential effects of procaine on frequency and amplitude of reticularly elicited hippocampal rhythmical slow activity. Hippocampus 3, 517–525.

Kjelstrup, K.B., Solstad, T., Brun, V.H., Hafting, T., Leutgeb, S., Witter, M.P., Moser, E.I., and Moser, M.B. (2008). Finite scale of spatial representation in the hippocampus. Science 321, 140–143.

Klausberger, T., Magill, P.J., Márton, L.F., Roberts, J.D., Cobden, P.M., Buzsáki, G., and Somogyi, P. (2003). Brain-state- and cell-type-specific firing of hippocampal interneurons in vivo. Nature 421, 844–848.

Kocsis, B., and Vertes, R.P. (1994). Characterization of neurons of the supramammillary nucleus and mammillary body that discharge rhythmically with the hippocampal theta rhythm in the rat. J. Neurosci. 14, 7040–7052.

Laurent, G. (2002). Olfactory network dynamics and the coding of multidimensional signals. Nat. Rev. Neurosci. 3, 884–895.

Lee, M.G., Chrobak, J.J., Sik, A., Wiley, R.G., and Buzsáki, G. (1994). Hippocampal theta activity following selective lesion of the septal cholinergic system. Neuroscience 62, 1033–1047.

Mathis, A., Herz, A.V., and Stemmler, M. (2012). Optimal population codes for space: grid cells outperform place cells. Neural Comput. *24*, 2280–2317.

Mattis, J., Tye, K.M., Ferenczi, E.A., Ramakrishnan, C., O'Shea, D.J., Prakash, R., Gunaydin, L.A., Hyun, M., Fenno, L.E., Gradinaru, V., et al. (2011). Principles for applying optogenetic tools derived from direct comparative analysis of microbial opsins. Nat. Methods *9*, 159–172.

McKenna, J.T., and Vertes, R.P. (2004). Afferent projections to nucleus reuniens of the thalamus. J. Comp. Neurol. *480*, 115–142.

Moser, E., Moser, M.B., and Andersen, P. (1993). Spatial learning impairment parallels the magnitude of dorsal hippocampal lesions, but is hardly present following ventral lesions. J. Neurosci. *13*, 3916–3925.

Moser, E.I., Kropff, E., and Moser, M.B. (2008). Place cells, grid cells, and the brain's spatial representation system. Annu. Rev. Neurosci. *31*, 69–89.

Mushiake, H., Sakamoto, K., Saito, N., Inui, T., Aihara, K., and Tanji, J. (2009). Involvement of the prefrontal cortex in problem solving. Int. Rev. Neurobiol. *85*, 1–11.

Nadel, L. (1968). Dorsal and ventral hippocampal lesions and behavior. Physiol. Behav. *3*, 891–900.

O'Keefe, J. (1991). An allocentric spatial model for the hippocampal cognitive map. Hippocampus *1*, 230–235.

O'Keefe, J., and Dostrovsky, J. (1971). The hippocampus as a spatial map. Preliminary evidence from unit activity in the freely-moving rat. Brain Res. *34*, 171–175.

Pan, W.X., and McNaughton, N. (2004). The supramammillary area: its organization, functions and relationship to the hippocampus. Prog. Neurobiol. *74*, 127–166.

Perez-Orive, J., Mazor, O., Turner, G.C., Cassenaer, S., Wilson, R.I., and Laurent, G. (2002). Oscillations and sparsening of odor representations in the mushroom body. Science *297*, 359–365.

Petsche, H., Stumpf, C., and Gogolak, G. (1962). [The significance of the rabbit's septum as a relay station between the midbrain and the hippocampus. I. The control of hippocampus arousal activity by the septum cells]. Electroencephalogr. Clin. Neurophysiol. *14*, 202–211.

Pfeiffer, B.E., and Foster, D.J. (2013). Hippocampal place-cell sequences depict future paths to remembered goals. Nature *497*, 74–79.

Royer, S., Sirota, A., Patel, J., and Buzsáki, G. (2010). Distinct representations and theta dynamics in dorsal and ventral hippocampus. J. Neurosci. *30*, 1777–1787.

Rutishauser, U., Ross, I.B., Mamelak, A.N., and Schuman, E.M. (2010). Human memory strength is predicted by theta-frequency phase-locking of single neurons. Nature *464*, 903–907.

Shimazaki, H., and Shinomoto, S. (2010). Kernel bandwidth optimization in spike rate estimation. J. Comput. Neurosci. *29*, 171–182.

Siapas, A.G., Lubenov, E.V., and Wilson, M.A. (2005). Prefrontal phase locking to hippocampal theta oscillations. Neuron *46*, 141–151.

Sigurdsson, T., and Duvarci, S. (2016). Hippocampal-prefrontal interactions in cognition, behavior and psychiatric disease. Front. Syst. Neurosci. *9*, 190.

Simon, N.W., Wood, J., and Moghaddam, B. (2015). Action-outcome relationships are represented differently by medial prefrontal and orbitofrontal cortex neurons during action execution. J. Neurophysiol. *114*, 3374–3385.

Singer, W. (1993). Synchronization of cortical activity and its putative role in information processing and learning. Annu. Rev. Physiol. *55*, 349–374.

Stemmler, M., Mathis, A., and Herz, A.V. (2015). Connecting multiple spatial scales to decode the population activity of grid cells. Sci. Adv. *1*, e1500816.

Stumpf, C., Petsche, H., and Gogolak, G. (1962). The significance of the rabbit's septum as a relay station between the midbrain and the hippocampus. II. The differential influence of drugs upon both the septal cell firing pattern and the hippocampus theta activity. Electroencephalogr. Clin. Neurophysiol. *14*, 212–219.

Thinschmidt, J.S., Kinney, G.G., and Kocsis, B. (1995). The supramammillary nucleus: is it necessary for the mediation of hippocampal theta rhythm? Neuroscience *67*, 301–312.

Vertes, R.P. (1992). PHA-L analysis of projections from the supramammillary nucleus in the rat. J. Comp. Neurol. *326*, 595–622.

Vertes, R.P., Crane, A.M., Colom, L.V., and Bland, B.H. (1995). Ascending projections of the posterior nucleus of the hypothalamus: PHA-L analysis in the rat. J. Comp. Neurol. *359*, 90–116.

Vertes, R.P., Hoover, W.B., Szigeti-Buck, K., and Leranth, C. (2007). Nucleus reuniens of the midline thalamus: link between the medial prefrontal cortex and the hippocampus. Brain Res. Bull. *71*, 601–609.

Wood, E.R., Dudchenko, P.A., Robitsek, R.J., and Eichenbaum, H. (2000). Hippocampal neurons encode information about different types of memory episodes occurring in the same location. Neuron *27*, 623–633.

Wouterlood, F.G., Saldana, E., and Witter, M.P. (1990). Projection from the nucleus reuniens thalami to the hippocampal region: light and electron microscopic tracing study in the rat with the anterograde tracer Phaseolus vulgaris-leucoagglutinin. J. Comp. Neurol. *296*, 179–203.

STAR★METHODS

KEY RESOURCES TABLE

REAGENT or RESOURCE	SOURCE	IDENTIFIER
Antibodies		
Rabbit monoclonal anti-NeuN	Abcam	Cat# ab177487; RRID: AB_2532109
Chicken polyclonal anti-GFP	Abcam	Cat# ab13970; RRID: AB_300798
Goat Anti-Chicken IgY H&L (Alexa 488)	Abcam	Cat# ab150169; RRID: AB_2636803
Goat anti-Rabbit IgG (H+L) Highly Cross-Adsorbed Secondary Antibody, Alexa 546	Thermo Fisher Scientific	Cat# A-11035; RRID: AB_2534093
Bacterial and Virus Strains		
AAV2-hSyn-eArch3.0-EYFP	University of North Carolina at Chapel Hill (UNC)'s gene therapy center	N/A
Chemicals, Peptides, and Recombinant Proteins		
Paraformaldehyde	Sigma	Cat# 158127
Cresyl Violet acetate	Sigma	Cat# C5042
Software and Algorithms		
MATLAB	MathWorks	https://www.mathworks.com/
MClust	A. David Redish	http://redishlab.neuroscience.umn.edu/MClust/MClust.html
Chronux	Partha Mitra	http://chronux.org/

CONTACT FOR REAGENT AND RESOURCE SHARING

Further information and requests for resources and reagents should be directed to and will be fulfilled by the Lead Contact, Hiroshi T. Ito (hiroshi.ito@brain.mpg.de).

EXPERIMENTAL MODEL AND SUBJECT DETAILS

Twenty-three male Long Evans rats (400–600 g at implantation) were housed individually in transparent Plexiglass cages (45 cm × 30 cm × 35 cm). Three of the rats were implanted with tetrodes in mPFC and CA1. Nine rats were implanted with tetrodes in both NR and CA1. The datasets from these twelve rats were used in our previous paper (Ito et al., 2015). Four rats had tetrodes in SUM. Seven rats received adeno-associated virus (AAV) injections in SUM; three of them had tetrodes in mPFC and CA1, and four of them had tetrodes in NR and CA1. All rats were kept at 85%–90% of free-feeding body weight and maintained on a 12-h light/12-h dark schedule. All behavioral training and recordings were performed in the dark phase. The experiments were performed in accordance with the Norwegian Animal Welfare Act and the European Convention for the Protection of Vertebrate Animals used for Experimental and Other Scientific Purposes.

METHOD DETAILS

Surgery, Virus Injection, Lesions, and Drive Implantation

The rats were anesthetized with isoflurane. Initial concentration in the induction chamber was 5.0% (vol/vol). Air flow was set to 1.0-1.5 l/min. For analgesia, Temgesic (buprenorphine, 15 μg/300 g; RB Pharmaceuticals Limited) was administered by subcutaneous injection. Following induction of anesthesia, the animal was fixed in a Kopf stereotaxic frame for electrode implantation and virus injection under 0.5%–2% isoflurane (vol/vol), adjusted according to physiological monitoring. Holes for tetrode implantation were drilled on the skull.

For tetrode recording from mPFC, animals were implanted with a 'hyperdrive' with 14 independently movable tetrodes constructed from 17-μm polyimide-coated platinum-iridium (90%–10%) wire (California Fine Wire). The tetrode bundle was circular. Thirteen tetrodes were implanted at anterior-posterior (AP): +3.25 mm from bregma, medial-lateral (ML): 0.6 mm from the midline, and dorsal-ventral (DV): 1.0 mm below dura, with a 5° lateral-to-medial angle in the coronal plane. One tetrode was targeted in the pyramidal layer of CA1 to record LFP (AP: −4.0, ML: 3.0, DV: 2.25). Electrode tips were plated with gold to reduce electrode impedances to 100–200 kΩ at 1 kHz. For simultaneous recording from NR and CA1, we used a split bundle of tetrodes, in order to independently target seven tetrodes (three independently movable double tetrodes and one reference) to NR (AP: −2.25, ML: 0.6) and seven tetrodes

(six independently movable tetrodes and one reference) to the hippocampus (AP: −3.25, ML: 2.5). The tetrodes were implanted with a 5° lateral-to-medial angle in the coronal plane. For tetrode recording from SUM and CA1, we used a split bundle of tetrodes to target seven tetrodes in SUM (AP: −4.25, ML: 0.6, with a 5° lateral-to-medial angle in the coronal plane) and seven tetrodes in CA1 (AP: −3.25, ML: 2.5). The hyperdrives were secured to the skull with jeweler's screws and dental cement. Two screws in the skull behind the lambda (above the cerebellum) were connected to the hyperdrive ground. Following the closure of the wound, the electrodes were turned into the cortex while signals were monitored on the recording system. The animals received an oral dose of the analgesic Metacam (Meloxicam, 0.1 mg per 300 g; Boehringer Ingelheim) during the first few days after the surgery.

For the optogenetics experiments, a solution of AAV2-hSyn-eArch3.0-EYFP virus (UNC vector core; University of North Carolina) was injected using a 10 μL NanoFil syringe and a 33-gauge beveled metal needle (World Precision Instruments) at two sites in SUM (AP: −4.25, ML 0.6 mm from the midline, DV: 8.25 and 7.75). The injection was made at a 5° lateral-to-medial angle in the coronal plane) in order to target the central portion of SUM in the coronal plane. Injection volume (0.5 μL at each site) and flow rate (0.05 μl/min) were controlled with a Micro4 Microsyringe Pump Controller (World Precision Instruments). After the injection, the needle was left in place for ten additional minutes before it was withdrawn slowly. After retraction of the needle, an optic fiber (FT400UMT: 0.39 NA, core size Ø 400 μm; Thorlabs) with two tetrodes attached was inserted so that the tip of the fiber was approximately 0.5 mm above SUM (AP: −4.25, ML: 0.6, DV: 7.5, with a 5° lateral-to-medial angle in the coronal plane). The two tetrodes were advanced 0.75 mm beyond the tip of the optic fiber, targeting SUM. The tetrodes were wired to the headstage connector for the recording system (Axona Ltd). After the optic fiber insertion, a hyperdrive was implanted on either mPFC or NR and CA1.

Electrode Turning and Recording Procedures

The hyperdrive was connected to a multichannel unity gain headstage (HS-54; Neuralynx). The output of the headstage was connected via a lightweight multi-wire tether and a Neuralynx PSR-36 commutator to a data acquisition system with 64-channel digital amplifiers (Digital Lynx; Neuralynx). Unit activity was filtered at 600 (64 taps)–6,000 (32 taps) Hz with an FIR band-pass filter. Spike waveforms above a threshold of ∼40 μV or more (noise r.m.s. < 20 μV) were time-stamped and digitized at 32,556 Hz at a 24-bit resolution for 1 ms. Light-emitting diodes on the headstage were tracked to obtain the animal's position and head direction. The local field potential (LFP) was filtered at 1–500 Hz with a running average filter (DCO) and a low-pass FIR filter (64 taps). The LFP signal was digitized at 2,034 Hz.

After the surgery, the tetrodes were moved in small daily increments toward the target area while the rat was resting on a pedestal. One electrode was used to record a reference signal from the superficial layers of the cortex (DV: ∼1 mm). The pyramidal cell layer of CA1 was identified during recording by the presence of sharp waves and large-amplitude complex-spike activity. On the day of recording, the electrodes were not moved at all to maintain stable recordings.

For tetrode recordings with optogenetic manipulations, a 532-nm light pulse was generated from a DPSS laser unit (Shanghai Laser & Optics Century) with a patch cable (FT400UMT; Thorlabs) connected to the animal. The laser power was 20–30 mW at the fiber tip. The laser application was controlled with a custom-made program in MATLAB (MathWorks) through an NI-DAQ system (USB-6211; National Instruments). Pulse delivery depended on the animal's position on the maze, which was monitored through a NetCom connection between MATLAB and Cheetah recording software (Neuralynx). Three to four weeks after the virus injection, silencing of cells with laser application was confirmed with tetrodes attached to the optic fiber. Unit activity from the tetrodes on the optic fiber was monitored using an Axona recording system (Axona Ltd). After the animals were sufficiently familiarized with the continuous alternation task, the first recording session (∼10 min) started with an optic-fiber patch cable connected to the animal without laser application. After the first session, the animal was at rest for 5 min before the next session, in which the light was applied for ∼10 min. To avoid unnecessary photodamage to the tissue, the laser application was turned off intermittently. The laser application was always on when the animal ran on the central stem and the side arms, but it was turned off when the animal reached the bottom arm. Five seconds after the animal reached the food port, the laser application was restarted, which was 8.11 ± 0.40 s (mean ± SEM) before the next run. The laser then continued to be on for the next trajectory. After the session with laser application, the animal was at rest in the Plexiglass home cage for ∼30 min before a new session was started. The final session (∼10 min) was conducted with the optic fiber patch cable connected without laser application.

Behavioral Task on the Modified T-Maze

The maze design was described previously (Ito et al., 2015). We used a modified T-maze with 110 cm × 110 cm square-shape, as shown in Figure 1A. The maze was constructed of 12 cm wide wooden runways covered by rubber sheet and with 2 cm high plastic side walls. Additional wall strips (10 cm length, 2 cm high, 1 cm thickness) were added on both sides at the end portion of the stem to reduce the width of the runway. This helped to minimize the lateral deviation of the animals' trajectories. Chocolate-taste cereals or cookies were provided on a small dish located at the center of the bottom arm. Reward was always given at the same spatial position, irrespective of whether the animals chose left or right trajectories, such that effects of intended movement could be dissociated from effects of the goal location itself. The maze was elevated 50 cm above the ground. It was surrounded by black circular curtains (180 cm diameter) without any visual cues on three sides. The bottom side of the maze was partially open to the recording room.

Behavioral training started after recovery from surgery. Training started with 1 or 2 days of accommodation where each rat was placed on the maze to freely explore and find food at the food port. In the next stage of training, the animals were instructed to follow a specific direction on the maze—from the stem through a side arm to the food port—by blocking reverse movement with

the experimenter's hands when necessary. Food was available at the food port irrespective of which trajectory the animal chose at this stage. After the animal was familiar with the movement direction rule on the maze, the final stage was to acquire the alternation rule. Reward was provided only when the animal chose the opposite trajectory of the previous trial, irrespective of whether choices were correct or incorrect on the preceding trial. For each day, three to five 10-min sessions were performed. Criterion was reached when choices were correct on 90% of the trials. Trajectory-dependent firing continued to be expressed long after the animals reached the behavioral criterion (for up to 2–3 months). Error trials were excluded in all analyses except for the analysis dedicated to error trials in Figure S2D.

Histological Procedures and Electrode Positions
The rats received an overdose of pentobarbital and were perfused intracardially with saline followed by either 4% formaldehyde (vol/vol). The brains were extracted and stored in formaldehyde, and frozen coronal sections (30 μm or 40 μm) were cut and stained with cresyl violet. Each section through the relevant brain region was collected for analysis. All tetrode and optic fiber traces were identified and the tip of each electrode was found by comparison across adjacent sections.

Immunohistochemistry
The brain sections were incubated overnight with 1:1000 concentration of anti-GFP (ab13970; Abcam) and anti-NeuN (ab177487; Abcam). The incubation was carried out at a temperature of 4 degrees in Tris-buffered saline containing 0.2% Triton X-100, BSA 2%, and NGS 4%, followed by 4 hr of secondary-antibody incubation with 1:1000 of Alexa 488-conjugated anti-chicken (Abcam) and 1:1000 of Alexa 546-conjugated anti-rabbit antibodies (ThermoFisher).

QUANTIFICATION AND STATISTICAL ANALYSIS

All statistical tests were two-sided. Data met assumptions about normality when parametric statistics were used.

Spike Sorting and Cell Classification
All main analyses were performed using MATLAB (MathWorks). Spike sorting was performed offline using MATLAB-based graphical cluster-cutting software, MClust (A.D. Redish). Clustering was performed manually in two-dimensional projections of the multidimensional parameter space (consisting of waveform energies and peak-trough amplitude differences). Autocorrelation and cross-correlation functions were used as additional separation tools. For recordings in CA1, putative pyramidal cells were distinguished from putative interneurons that were classified by a criterion of mean firing rates > 5 Hz on both stem and nonstem regions. The results of this classification matched with previously described differences in spike width and average rates of pyramidal neurons and interneurons (putative pyramidal neurons: spike half-width 152.5 ± 2.3 μs, peak-trough time 299.5 ± 9.2 μs, mean firing rates 1.83 ± 0.13 Hz; putative interneurons: spike half-width 134.6 ± 3.8 μs, peak-trough time 189.9 ± 9.0 μs, mean firing rates 13.9 ± 1.12 Hz; e.g., Csicsvari et al., 1999). Only cells with a peak firing rate more than 1 Hz on the central stem of the maze on either trajectory were analyzed.

To ensure the same cell was not counted multiple times, for recordings in CA1, the estimated number of cells recorded on each tetrode was based on a single recording session (with tetrodes placed optimally in the cell layer). For recordings from mPFC, NR or SUM, discrete units were sampled from recording sessions with at least 40 μm separation from the preceding and succeeding recording locations.

Trajectory-Dependent Firing on the Modified T-Maze
For analysis of trajectory-dependent firing on the stem, we first extracted a portion of the stem where the animal's running speed, head direction, and lateral position were not significantly different between left and right trajectories. Ninety-five percent confidence intervals for multiple comparisons of six bins (with Bonferroni correction) were determined for lateral position on left- and right-turn trajectories and the portion of the central stem with overlapping confidence intervals was extracted for analysis. A segment of 5 cm was further excluded from the end of the extracted stem portion to guarantee minimal trajectory deviation.

To analyze trajectory-dependent firing on the central stem of the T-maze, we divided it into six equally sized bins. The length of individual bins was 8–13 cm, depending on the selected portion of the stem. The following parameters were calculated for each bin of each trial: (1) firing rate: the number of spikes divided by the amount of time spent in the bin; (2) running speed: the averaged position shift per time in the bin; (3) head direction: the averaged angle of two colored LEDs on the headstage; and (4) lateral position: averaged position perpendicular to the long axis of the central stem.

For each cell, a two-way ANOVA was conducted with trial type (correct left- and right-turn run) and six bins as independent variables and firing rate as the dependent measure. In the hippocampus, cells with a significant main effect of trial type were identified as potential trajectory-dependent cells. For these cells, a second analysis was performed to examine whether variations in speed, heading, or lateral position might account for the differences in firing rate between trial types. This was examined with a two-way ANCOVA with trial type and bins as the independent variables, firing rate as the dependent measure, and speed, head direction, and lateral position as covariates. Cells that continued to show a significant difference in firing rate between left- and right-turn trials, when the covariates were included in the ANCOVA model, were classified as trajectory dependent (Wood et al., 2000). For neurons in

mPFC, NR or SUM, any cell which showed either a significant main effect of trial type or a significant trial type × bin interaction with both ANOVA and ANCOVA, was considered a trajectory-dependent cell.

To create spatial rate maps, spatial positions in the maze were divided into 10 × 10 pixel bins (3 pixels per cm) and the firing rate for each bin was calculated. This was performed only for periods when the animal's running speed exceeded 10 cm/s. Instantaneous spike rates were estimated using a Gaussian kernel on the spike data for temporal smoothing. Instantaneous rate was calculated as

$$r(t) = \sum_{i=1}^{N} g\left(\frac{t_i - t}{h}\right)$$

where g is a 1D Gaussian kernel, *h* is a bandwidth, *N* is the total number of spikes, and t_i is the time of the i-th spike. An optimal bandwidth between 50 and 250 ms was determined for each cell by minimizing the mean integrated square error between the estimated rate and the unknown underlying rate (Shimazaki and Shinomoto, 2010). The rate map was smoothed using a 2D Gaussian filter with a bandwidth of one bin (3.3 cm × 3.3 cm). Bins visited less than 40 ms were excluded. Spike rate at each stem position was estimated using a linear interpolation method applied to temporally smoothed spike rates by the 1D Gaussian kernel.

Spike Phase Analysis

Spike-field coherence is the ratio of the power spectrum of the spike-triggered LFP average and the average power spectrum of the LFP traces that were used to construct the spike-triggered LFP average (Fries et al., 2001). Spike-field coherence takes values from 0% to 100%. The spike-triggered LFP average was constructed by extracting LFP segments of 300 ms centered at the spike timing. The signal power at different frequencies was estimated by a wavelet convolution method using complex morlet wavelets with frequencies ranging from 4 to 140 Hz at 2 Hz intervals (Colgin et al., 2009). We only considered spikes that were elicited when the animal's running speed was above 10 cm/s. Neurons that did not elicit more than 20 spikes in either the stem or nonstem regions during the entire session were excluded from the analysis. We also used another method based on the Hilbert transform to estimate spike-phase locking. The signal was first filtered by a band-pass FIR filter that was designed by Parks-McClellan algorithm at a specific frequency range (pass band for theta: 6-12 Hz, slow gamma: 25-45 Hz, fast gamma 65-90 Hz), then the Hilbert transform was applied to estimate phases and amplitudes of oscillations in the filtered frequency range. We then constructed a circular histogram of spike phases and examined its mean vector length.

Because both of these spike-phase estimation methods are dependent not only on the degree of spike-phase coupling but also on the number of spikes used to calculate them (Rutishauser et al., 2010), the number of spikes was always equalized for the group comparison (e.g., between the stem and nonstem, or among before, during, and after laser application). We used a bootstrap resampling procedure for this purpose. We set the sampling number of spikes to be 4/5 of the minimum number of spikes across the groups. Then, we randomly chose the same number of spikes from each group to estimate spike-field coherence or mean vector length, which was repeated 25 times and their averages was considered as a representative value of the group.

For the normalization of the animal's running speed between the stem and nonstem parts of the maze, we compared the average of instantaneous running speed when spikes are generated. Then, spikes of the group with a higher mean running speed were sorted according to instantaneous running speed at the spike timing, and excluded the spike that was elicited at the highest running speed one by one until we could reach the same average running speed between the groups. After this procedure, the bootstrap resampling procedure was implemented to equalize the number of spikes between the groups, as described in the previous paragraph.

For the phase precession analysis, theta phases at the time of spiking were plotted across positions in the place field for each cell. The degree of phase precession was evaluated based on slopes of fitted-lines on the plots by circular-linear regression (Kempter et al., 2012).

For the spike-time cross-correlation analysis for pairs of neurons, spike-time correlation plots were generated at 10-ms bins, and the time difference that gave the maximum correlation was evaluated for each cell pair. The correlation plots were then normalized and averaged across all cell pairs.

Spectral Coherence Analysis

Spectral coherence between LFPs was calculated using a multitaper method using the Chronux toolbox (http://chronux.org) with the time-bandwidth product of 3 and 5 tapers. The sliding window was 512 ms in size and was advanced by 100 ms.

Decoding Analysis

Decoding performance was estimated using a population vector decoder and a leave-one-out cross-validation procedure, performed as follows. From a given set of trials in a recording session, one trial was randomly chosen as a test dataset, and the rest of the trials were used as a training dataset. Firing rates of each neuron were normalized to z scores. Population vectors of mean firing rates on the stem were calculated separately for right- and left-trajectory trials on the training dataset. The trajectory choice represented in the same population of neurons on the test dataset was estimated by the following equation.

$$T = sign\left(\mathbf{v} \cdot c_{right} - \mathbf{v} \cdot c_{left}\right)$$

in which c_{right} and c_{left} are the population vectors from the training dataset for right- or left-trajectory trials, and v is a vector of firing rates of the same population of neuron on the test dataset. T is the output value of the classifier; 1 or −1 represents right- or left-trajectory, respectively. This procedure was repeated for all trials to be tested, and the classification accuracy on the test datasets was considered an estimate of the decoding performance. To estimate decoding performance of a specific number of neurons, we randomly selected a given number of neurons across all recording sessions. As the total trial number was usually different across sessions, we randomly selected trials to equalize them. This procedure was repeated 1000 times to obtain a statistical distribution of decoding performance (bootstrap resampling method).

Signal Directionality Analysis

The directionality of signal flow was estimated by examining the microstructure of coupling between the CA1 theta and the spike activity in another brain region. The mean vector lengths of spike phases were calculated for each cell relative to a series of CA1 LFP traces that were band-pass filtered at 6 −12 Hz and temporally shifted from −200 ms to 200 ms at 10 ms intervals relative to the original trace. We identified the temporal shift that gives the maximum mean vector length, which is considered to provide a good estimate of signal directionality (Siapas et al., 2005). These optimal time shifts obtained from individual neurons were used for statistical analysis. Cells without the maximum peak of mean vector length in the range of temporal shift between −200 ms to 200 ms were excluded from the analysis. For the visualization in Figure 5B, the mean vector length was normalized for each cell and averaged across the population.

Theta Waveform Analysis

The beginning and end of individual theta cycles were extracted from unfiltered LFP based on the times when instantaneous phases, estimated by a Hilbert transform of the filtered LFP at the theta-frequency range, returned to zero degree.

Sharpness at the peak of theta oscillation was calculated using the following equation (Cole et al., 2017).

$$Sharp = \frac{(V_{Peak} - V_{Peak-5ms}) + (V_{Peak} - V_{Peak+5ms})}{2}$$

Sharpness at the trough was evaluated similarly, and the ratio of the peak and trough sharpness was obtained for individual theta cycles.

Detection of Theta Rhythmicity

The spike-time autocorrelogram was generated at 10-ms bins up to 400 ms lags. Each autocorrelogram was fit with the following equation (Royer et al., 2010; Brandon et al., 2013).

$$y(x) = [a(cos(wx) + 1) + b] \times exp\left(-\frac{|x|}{\tau_1}\right) + c \cdot exp\left(-\frac{x^2}{\tau_2^2}\right)$$

where w is considered as a frequency of rhythmicity. A cell was considered as theta rhythmic when the 95% confidence intervals of w were within the range of 6 to 12Hz.

DATA AND SOFTWARE AVAILABILITY

Data and code are available upon request to the Lead Contact.